


Controlling Antiferromagnetic Magnon Polarization by Interfacial Exchange Interaction

Yawen Liu,^{1,†} Haoyu Liu,^{1,†} Wei Yuan^{①,1}, Yuhang Li,² Junxue Li^{①,1}, Qiming Shao^{①,3}, Ran Cheng^{①,2,1} and Jing Shi^{①,1,*}

¹*Department of Physics and Astronomy, University of California, Riverside, California 92521, USA*

²*Department of Electrical and Computer Engineering, University of California, Riverside, California 92521, USA*

³*Department of Electronic and Computer Engineering, The Hong Kong University of Science and Technology, Hong Kong, China*

 (Received 28 September 2021; revised 2 May 2022; accepted 22 July 2022; published 2 September 2022)

We demonstrate highly efficient control of antiferromagnetic (AFM) magnon spins by the interfacial exchange interaction in heterostructures of ferrimagnetic yttrium iron garnet (YIG) and AFM Cr₂O₃. At low temperatures, Cr₂O₃ is antiferromagnetically ordered. The interfacial exchange interaction exerted by YIG lifts the degeneracy between the AFM magnon modes in Cr₂O₃, resulting in a net spin polarization and a spin current dominated by left-handed magnons, even at zero magnetic field, which is detected by the spin Seebeck effect with a 5-nm-thick Pt film. In the AFM magnon-dominated region, even if the magnetic field is not sufficiently strong to induce the spin-flop transition in Cr₂O₃, the total spin Seebeck signal polarity flips when the YIG magnetization switches. It clearly indicates that the Cr₂O₃ magnon polarization is controlled by YIG magnetization through the interfacial exchange interaction. The demonstration of the efficient control of AFM magnon polarization opens a pathway to manipulate AFM magnon quantum states using FM-AFM heterostructures.

DOI: [10.1103/PhysRevApplied.18.034005](https://doi.org/10.1103/PhysRevApplied.18.034005)

I. INTRODUCTION

Magnons, the sole carriers of angular momentum in insulating magnetic solids, have been actively explored for energy-efficient magnon-based spintronics in recent years [1–3]. Owing to the intrinsically ultrafast spin dynamics and robustness against magnetic field perturbations, antiferromagnetic (AFM) insulators have become a particularly interesting focus of recent studies [4–14]. Analogous to electrons in metallic ferromagnets (FMs), magnons in collinear AFMs have two quantum spin states associated with the two eigenmodes corresponding to opposite chiralities in spin precession, as shown in Fig. 1(a) [15–18]. This is distinctly different from magnons in FMs, where only the right-handed chirality is present, which always gives rise to finite spin polarization. In AFMs, spin polarization and magnon spin currents can be induced when the degeneracy between the two eigenstates is lifted, similar to electrons in metallic FMs.

Recent experimental studies have established the electrical detection of AFM magnon spin currents in uniaxial AFMs generated either thermally (i.e., spin Seebeck effect or SSE) or resonantly (i.e., AFM spin pumping) [4–13]

under a large external magnetic field, H . In SSE measurements, when H is applied parallel to the Néel vector with the magnitude below the spin-flop (SF) threshold, the left-handed magnon states (β mode) with the magnetic moment down (parallel to H) are more populated than the right-handed magnon states (α mode), resulting in a net spin density and a magnon spin current in the presence of a temperature gradient. The SSE signal flips sign when H exceeds the SF threshold because the AFM ground state gives way to a quasi-FM spin configuration [13]. However, a large H in excess of 1 T is often required to induce an appreciable spin current. The AFM spin pumping suffers from the same drawback. Here, we propose a FM-AFM heterostructure approach that leverages the interfacial exchange coupling. Different from the well-known exchange-bias effect [19] in FM-AFM, here, it is the reverse effect of the same interaction that we are exploiting to manipulate AFM magnon spin currents, not simply the static spin configurations. Namely, we deal with the back action of the same interfacial exchange bias on the AFM magnon quantum states or the dynamic properties of the AFM layer by the FM layer. We demonstrate that the AFM magnon dispersions can be controlled by a relatively weak magnetic field that is strong enough to alter the FM magnetization. A similar interfacial exchange-interaction effect is adopted to

*jing.shi@ucr.edu

†Y. Liu and H. Liu contributed equally to this work.

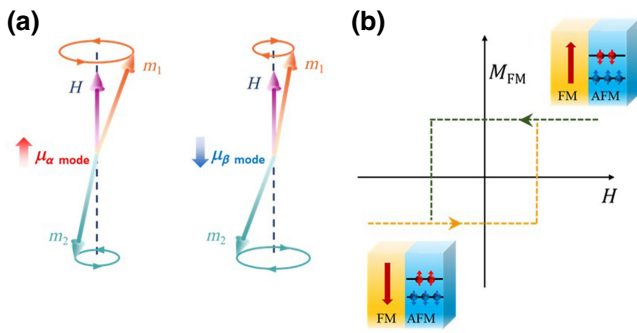


FIG. 1. (a) Illustration of two magnon eigenmodes in colinear antiferromagnet: α and β modes, each with magnetic moment μ . Throughout the paper, arrows indicate magnetic moment directions of electrons, which differ from the spin-polarization directions by a minus sign. (b) Exchange interaction from FM acts on AFM as a static biasing field and lifts the degeneracy of α and β modes even at $H=0$. As FM magnetization reverses, the quantization axis for AFM magnons flips accordingly.

induce a time-reversal breaking mechanism by the FM in FM-nonmagnetic heterostructures, but on the static spin properties [20–26].

II. FM-AFM HETEROSTRUCTURES AND SSE MEASUREMENTS

In a FM-AFM heterostructure, the FM layer acts effectively as the source of a biasing magnetic field, which lifts the degeneracy of the two eigenmodes of the AFM layer, as shown in Fig. 1(b). With respect to the FM magnetization direction, the β -mode magnons (moment down or μ_β mode) in the AFM layer dominates the magnon spin current due to their lower energy. Upon flipping the FM magnetization, the polarization direction of the β -mode magnons reverses accordingly. The left-handed β -mode magnons populated in the AFM layer compete with the right-handed magnons generated in the FM layer. This competition may lead to a sign change of the inverse spin Hall effect (ISHE) voltage in a heavy-metal layer placed on top of the AFM layer.

We use the material structure shown in Fig. 2(a) to investigate the aforementioned effect. We first grow a 10–15-nm-thick single-crystalline ferrimagnetic yttrium iron garnet (YIG or $\text{Y}_3\text{Fe}_5\text{O}_{12}$) layer on (110)-oriented gadolinium gallium garnet (GGG or $\text{Gd}_3\text{Ga}_5\text{O}_{12}$) substrates using pulsed laser deposition. Typical growth conditions for high-quality epitaxial YIG films can be found elsewhere [27]. To grow Cr_2O_3 films on YIG, we explore a variety of growth conditions, including different growth temperatures, laser energies, growth times, and postgrowth annealing temperatures and durations. The film quality is characterized by *in situ* reflection high-energy electron diffraction (RHEED), atomic force microscopy, high-resolution transmission electron microscopy (HRTEM), and energy-dispersive x-ray spectroscopy (EDX). We

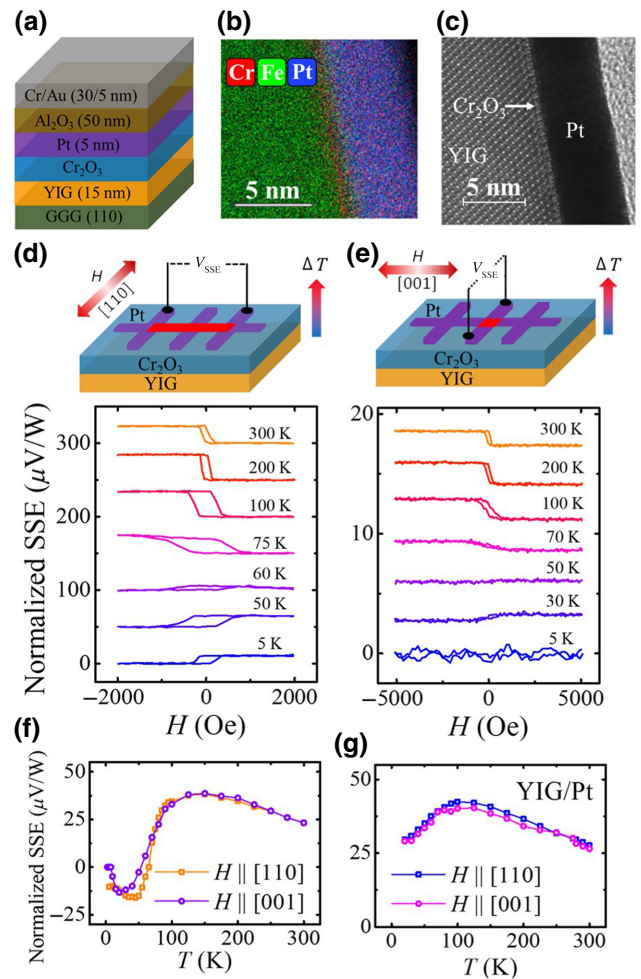


FIG. 2. (a) Material stack for YIG/ Cr_2O_3 /Pt SSE devices. (b),(c) EDX and HRTEM images of ML- Cr_2O_3 sample. (d),(e) SSE device schematic (upper) and normalized SSE loops (lower) at selected temperatures measured in two orthogonal orientations. (f) Temperature dependence of SSE at saturation (2 kOe). Due to Pt-length difference, the $H||\text{YIG}$ [001] curve is manually rescaled to match the $H||\text{YIG}$ [110] curve at 300 K. Error bar represented by the standard deviation for 5-K data (noisiest) is about the size of the symbols shown in the figure. (g) Temperature dependence of SSE at saturation (2 kOe) in the YIG/Pt control sample.

identify a narrow growth temperature window between 400 and 600 °C that yields reasonably smooth polycrystalline Cr_2O_3 films but results in a very slow growth rate (~ 5 – 10 nm/h). Postgrowth annealing above 750 °C, by either a furnace or rapid thermal annealer, further improves the film crystallinity but generally increases the film roughness, as tracked by RHEED and atomic force microscopy. We find that the final film thickness also depends on the annealing time, in addition to other factors, such as the growth temperature and laser energy. Due to the sensitivity to the large number of parameters, we generally obtain Cr_2O_3 films over a range of thicknesses (0.73–15 nm). The thinnest Cr_2O_3 in our sample set is a monolayer (ML)

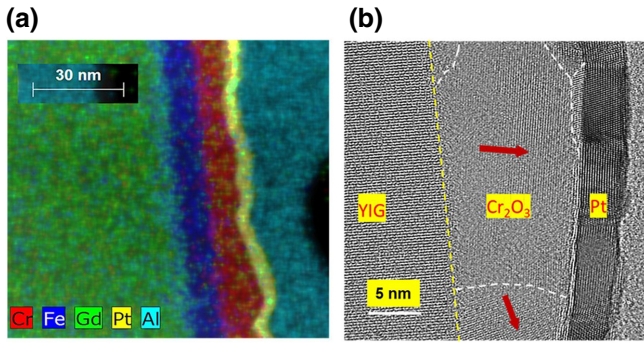


FIG. 3. EDX mapping (a) and HRTEM (b) image of the cross section of YIG/Cr₂O₃(12 nm)/Pt device. From left to right, layers are GGG, YIG, Cr₂O₃, Pt, and Al₂O₃ in (a); and YIG, Cr₂O₃, Pt, and Al₂O₃ in (b). Polycrystalline grains in Cr₂O₃ can be seen in the HRTEM image, and arrows represent the *c*-axis direction in two representative grains.

with a thickness of 0.73 nm, as determined from these images [Figs. 2(b) and 2(c)], denoted as ML-Cr₂O₃. Similar images on a representative of thick samples are shown in Fig. 3. The HRTEM image of the 12-nm Cr₂O₃ sample [Fig. 3(b)] reveals the polycrystalline nature of the film, with the *c* axis oriented off the surface normal of the interface.

After growing Cr₂O₃ films on YIG, we deposit a 5-nm-thick Pt layer on top using magnetron sputtering. We form two different sets of Pt patterns, as schematically shown in Figs. 2(d) and 2(e) (channel width of 100 or 200 μm and length ranging from 2 to 4 mm) by photolithography and inductively coupled plasma etching. The etched Pt pattern is covered by a 50-nm-thick Al₂O₃ insulating layer grown by atomic layer deposition followed by a 30-nm Cr/Au heater layer deposited using *e*-beam evaporation. The heater-layer pattern is formed by photolithography and liftoff and aligned to the etched Pt pattern underneath.

We perform SSE measurements in Quantum Design's DynaCool physical property measurement system and Janis' 4-K closed-cycle system down to a temperature of 4 K. In the SSE measurements, we use a Keithley 6221 ac source meter to apply an ac current with a constant amplitude in the Cr/Au heater, a Keithley 2000 voltmeter to measure the ac voltage across the heater, and SR830 locked-in amplifiers combined with SR560 preamplifiers to detect the ISHE voltages from the Pt channels. We typically set the frequency of the heating current at 17 Hz, then measure the double-frequency SSE signals at 34 Hz. The signals are amplified by 1000 times with the SR560 preamplifier.

III. SSE IN HETEROSTRUCTURE WITH ML-Cr₂O₃

As shown in the top panels of Figs. 2(d) and 2(e), we perform SSE measurements with the in-plane magnetic

field, H , set along two orthogonal directions in the ML-Cr₂O₃ device. To obtain maximum SSE responses, we record the voltage in the Pt channel that is oriented perpendicular to H . In the low-field regime (<2 kOe), the field strength is sufficiently large to saturate the YIG magnetization but insufficient to change the Néel vector of Cr₂O₃. The bottom panels of Figs. 2(d) and 2(e) display the measured ISHE voltage normalized by heating power as a function of H at selected temperatures for both orientations. A common feature in the two sets of SSE data is that the loop becomes inverted at and below 60 K. The loop inversion is clearly illustrated by plotting the normalized ISHE voltage at saturation versus temperature, as shown in Fig. 2(f). In contrast, the SSE of the YIG/Pt control sample does not change sign throughout the entire temperature range; therefore, here, we use the YIG/Pt loop as our SSE reference and define its SSE sign as positive [Fig. 2(g)]. In comparison, the SSE signal from YIG/Cr₂O₃/Pt is positive at room temperature, which is expected because ML-Cr₂O₃ is paramagnetic at 300 K, and therefore, the total SSE signal should originate from the transmitted and attenuated spin current generated in the YIG layer. At lower temperatures, however, Cr₂O₃ orders antiferromagnetically, so we expect a change in the total SSE behavior. Therefore, we attribute the observed SSE sign change to the AFM ordering of Cr₂O₃. When H is applied along the [110] direction, the sign change occurs at about 65 K and remains negative below this point. When H is applied along the [001] direction, the sign change occurs at about 53 K, and the signal vanishes below 10 K. In a previous study, Qiu *et al.* reported that the propagation of FM magnons was blocked by an AFM Cr₂O₃ layer, the Néel vector of which was perpendicular to the polarization of FM magnons [28]. We do not observe sharp shutoff of the SSE signal below T_N . As discussed below, the in-plane *c*-axis configuration explains the negative signal due to the AFM β -mode magnons [9,10,29,30].

To understand the contribution from the AFM magnons, we first determine the T_N of the ML-Cr₂O₃ film from our SSE measurements. In general, we expect an enhanced SSE near T_N due to critical fluctuations [9]. In YIG/Cr₂O₃ heterostructures, this critical anomaly of Cr₂O₃ is superimposed on the YIG/Pt SSE background, which makes it difficult to cleanly separate the two. However, we observe a peak at about 150 K in the ML-Cr₂O₃ sample, which occurs about 50 K higher than the YIG/Pt SSE peak; therefore, we identify 150 K as the T_N of the ML-Cr₂O₃ film [Fig. 4(a)]. Below T_N , as the long-range AFM order is established, the β -mode AFM magnons become an additional spin-current source and can dominate spin transport due to direct contact with Pt. In AFM materials alone, however, nonzero equilibrium spin polarization can only be induced by a magnetic field. At low temperatures, where the negative squared SSE hysteresis loops in YIG/Cr₂O₃/Pt are observed, two zero-field β -mode

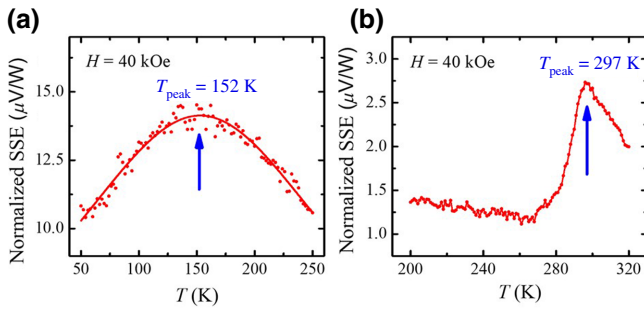


FIG. 4. Temperature dependence of the SSE voltage normalized by heating power V_{SSE}/P for $\text{Y}_3\text{Fe}_5\text{O}_{12}/\text{ML-Cr}_2\text{O}_3/\text{Pt}$ (a) and $\text{Y}_3\text{Fe}_5\text{O}_{12}/\text{Cr}_2\text{O}_3$ (12 nm)/Pt (b). Relatively broad peak centers around 152 K in the ML- Cr_2O_3 sample (a). In the 12-nm Cr_2O_3 sample (b), the peak shifts to 297 K, closer to the T_N of bulk Cr_2O_3 crystals. Similar SSE anomaly at T_N is observed in standalone Cr_2O_3 films (without YIG) with various thicknesses ranging from 7 to 100 nm, indicating the critical fluctuation origin of the peak.

magnon polarizations exist. This is only possible when Cr_2O_3 is subjected to a strong effective field, which stems from the exchange coupling. At the YIG/ Cr_2O_3 interface, the exchange coupling plays the role of the external field and lifts the degeneracy of the two AFM magnon eigenmodes in ML- Cr_2O_3 . If the exchange coupling is ferromagneticlike, it makes the thermal excitation of the β mode energetically favorable. Spin polarization of such β -mode magnons is along the magnetization of the YIG, hence opposite to the spin polarization of the FM magnons. When H exceeds the coercive field, H_C , of YIG, its magnetization switches, so does the quantization axis of the AFM magnons, resulting in a SSE hysteresis loop. Via a strong exchange interaction, a small external magnetic field (e.g., ~ 100 Oe) can reverse the AFM spin polarization, as long as $H > H_C$ of YIG, and retain it even at $H = 0$. Between the two orthogonal in-plane field directions, i.e., YIG [110] and YIG [001], we observe a similar characteristic temperature dependence, such as the negative SSE over approximately the same temperature range, as shown in Fig. 2(f), indicating a distribution along the in-plane c -axis orientation in the ML- Cr_2O_3 film.

In this low-field regime, the spin state in Cr_2O_3 is essentially untouched by H . To investigate the field responses of Cr_2O_3 , we measure SSE data by extending the maximum H to 60 kOe. A set of representative high-field SSE hysteresis loops is displayed in Fig. 5(a), which also contains the low-field data previously shown in Fig. 2. While the low-field loops undergo a sign change as the temperature is lowered, the high-field SSE signals remain positive over the entire temperature range. At high temperatures, where the low-field SSE signal is positive, the high-field response is a mere extension of the already saturated signal. At low temperatures, however, the overall field dependence can

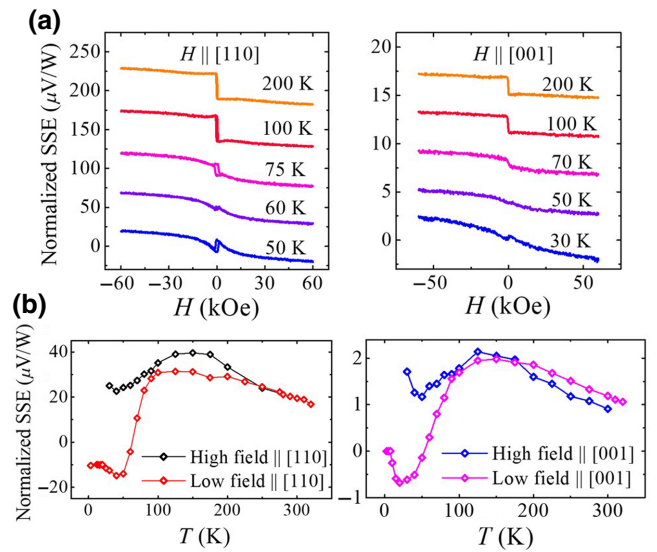


FIG. 5. (a) Normalized SSE hysteresis loops in YIG/ML- $\text{Cr}_2\text{O}_3/\text{Pt}$ measured up to 60 kOe. (b) Comparison of low-field (2 kOe) and high-field (60 kOe > SF field) SSE signals in both [110] and [001] field orientations. Error bar represented by the standard deviation for the 30-K high-field data (noisiest) is about the size of the symbols shown in the figure.

be viewed as a superposition of two signals: a negative low-field hysteresis loop and a positive high-field background. Above the saturation field of the low-field loop, much higher fields (i.e., in excess of 60 kOe) are needed to bring the total SSE signal to saturation. It is noteworthy that at lower temperatures the low-field SSE loop inversion is accompanied by higher fields required to reach saturation. Figure 5(b) compares the temperature dependences of the SSE signals taken at low (2 kOe) and high (60 kOe) fields in both field orientations. Clearly, as the temperature is lowered, a significant discrepancy between the two field regimes starts to emerge below T_N but preceding the SSE sign change. On the other hand, the high-field SSE shows a similar all-positive trend to that in YIG/Pt, except that the peak in the former is broader than that in the latter. The broader high-field SSE temperature-dependence peak may be composed of the YIG SSE peak at about 100 K [Fig. 2(g)] and the critical peak of Cr_2O_3 near $T_N \sim 150$ K [Fig. 3(a)]. For the grains with the c axis parallel to YIG magnetization, the β -mode magnon contribution, i.e., the negative SSE, is suppressed as H approaches the SF field. We note that, because of the lower T_N in ML- Cr_2O_3 , the AFM exchange strength and, consequently, the SF field will be reduced compared to Cr_2O_3 bulk crystals. An even higher H than the SF field causes spins to flop and induces a canted moment, which drives the Cr_2O_3 SSE toward positive sign because of the right-handed magnon contribution. For the c -axis orientations not parallel to YIG magnetization, a canted moment exists, even at low H .

Additionally, in this canted spin configuration, more FM magnons from YIG can reach the Pt layer mediated by the canted magnetic moments in Cr_2O_3 . Consequently, a larger YIG spin current is transmitted through the larger field-induced canted moments and produces a larger positive SSE signal. It is interesting to note that the high-field SSE voltage magnitude in Fig. 5(b) shows an upturn at low temperatures. A similar trend was previously observed in other systems [31] and is likely due to the high-field-induced magnon-thermal-conductivity suppression at low temperatures.

IV. SSE IN HETEROSTRUCTURE WITH 12-nm-THICK Cr_2O_3

To further confirm the above AFM magnon picture, we now turn to YIG/ Cr_2O_3 /Pt devices with thicker Cr_2O_3 layers. Here, we show the results from the 12-nm-thick polycrystalline Cr_2O_3 sample for which the EDX and HRTEM results are shown in Fig. 3. The SSE temperature dependence for H along YIG [110] is shown in Fig. 4(a). The T_N of this 12-nm-thick Cr_2O_3 film is found to be about 300 K, closer to the bulk T_N of 308 K [see Fig. 4(b)]. Similar to the ML sample, the SSE signal is positive at high temperatures (here, $T > 300$ K). As the temperature decreases, the SSE peaks at 300 K are followed by a sharp decline. The much-reduced positive SSE signal continues decreasing in magnitude and passes zero at about 200 K. Then it stays negative until about 80 K, below which the signal becomes too small to be detected. As mentioned earlier, the similar sharp decline of the SSE reported by Qiu *et al.* [28] is interpreted as a shutoff of the incoming spin current in YIG by the frozen AFM moments below T_N when the Néel vector of Cr_2O_3 is perpendicular to the FM magnon polarization. Here, in addition to the precipitous drop, we can still well resolve the much smaller positive and negative SSE signals below T_N that are not observed in Refs. [28,32]. It is interesting that both the monolayer and 12-nm samples have a negative SSE region. Based on these observations, we arrive at the following explanation. In ML- Cr_2O_3 , the c axis is in-plane, together with which the in-plane interfacial exchange field produces the negative SSE, as previously discussed. In contrast, the 12-nm polycrystalline film develops a significant fraction of grains with the out-of-plane c axis [representative image shown in Fig. 3(b)]. These grains block the spin current from YIG, as in Ref. [28], which results in a much-reduced SSE signal from the remaining grains with the in-plane c axis. Such structural differences between the ML and thick Cr_2O_3 films can arise from film growth. In thicker Cr_2O_3 films, the interfacial constraint is weaker; consequently, more grains can adopt the out-of-plane c -axis orientation.

In FM-AFM bilayers, the interfacial exchange is often revealed by a shifted hysteresis loop of the FM layer. In the thick Cr_2O_3 sample, we indeed observe shifted hysteresis

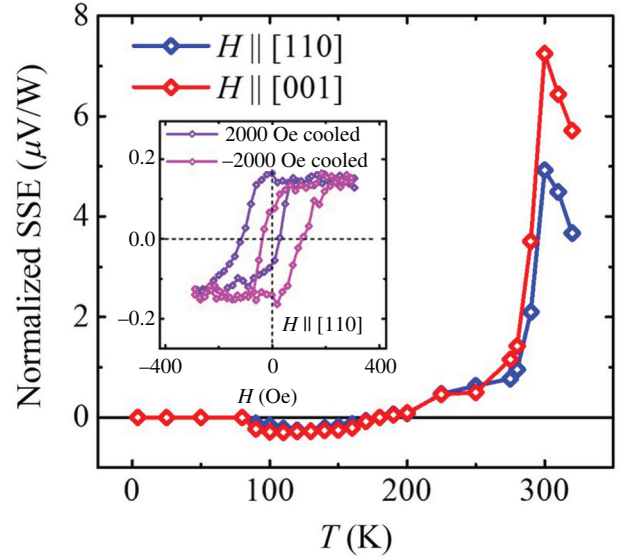


FIG. 6. Temperature dependence of saturated SSE magnitude for both field orientations. Inset shows shifted SSE loops in YIG/ Cr_2O_3 (12 nm)/Pt after field cooling along YIG [110] performed in the negative SSE region.

loops, as shown in the inset of Fig. 6, by performing field cooling from 320 K in constant fields, +2000 and -2000 Oe, respectively. In the negative SSE region, a loop shift of about 80 Oe is clearly visible, which is indicative of the exchange-bias effect [19,33]. Not only is this loop shift a confirmation of antiferromagnetism in our Cr_2O_3 films, but also validates the reverse exchange-bias effect on Cr_2O_3 , which has exactly the same interfacial origin as that in the shifted YIG hysteresis loops.

V. THEORETICAL MODELING RESULTS

We formulate an intuitive theory to uncover the essential physics underlying the sign change of the magnon SSE. Since both the YIG and Cr_2O_3 are thin films, magnon modes are highly quantized due to geometric confinement; hence, the diffusive transport picture, in which T can be viewed as a continuous function [34], does not apply. Instead, we assume that the temperature drop, ΔT , primarily takes place across the interface of Cr_2O_3 and Pt because of the thermal conductivity mismatch, whereas T essentially remains constant inside the YIG and Cr_2O_3 thin layers. The SSE signal is then proportional to the interfacial nonequilibrium spin density, δS_z . To calculate the ratio $\delta S_z / \Delta T$ as a function of T , we first need to obtain the magnon-band structures in FM-AFM heterostructures. We adopt a lattice model and describe the system by the Heisenberg Hamiltonian, $H = H_{\text{FM}} + H_{\text{AFM}} + H_T$, where $H_{\text{FM}} = J_F \sum_{\langle ij \rangle} \mathbf{S}_i \cdot \mathbf{S}_j + K_F \sum_i S_{iz}^2$ describes the YIG layer, $H_{\text{AFM}} = J_A \sum_{\langle ij \rangle} \mathbf{S}_i \cdot \mathbf{S}_j + K_A \sum_i S_{iz}^2$ describes the Cr_2O_3 layer, and $H_T = J_t \sum_{x,y} \mathbf{S}_{x,y,N_F} \cdot \mathbf{S}_{x,y,N_F+1}$ is the

exchange Hamiltonian of the FM-AFM interface. Here, J_F (J_A) and K_F (K_A) are the exchange coupling and uniaxial anisotropy of the FM (AFM) subsystem, and J_t denotes the exchange coupling between the coupled FM and AFM layers. Without loss of generality, we consider a simple cubic lattice and assume periodic boundary conditions in the lateral dimensions (i.e., x and y directions). The layer number along the plane normal (i.e., z direction) is N_F (N_A) for the FM (AFM) layer. Using the Holstein-Primarkoff transformation and a Fourier transformation, we diagonalize the Hamiltonian and numerically solve the band structure [35]. We obtain three distinct bands, arising from the hybridization of FM and AFM magnons, as schematically illustrated in Fig. 7. Magnons in the lowest band are localized inside the FM and have only a small probability of interacting with the electrons from Pt (on the rightmost boundary). The other two bands originate from the α and β modes carrying opposite spins; these bands are split in energy by the exchange interaction, J_t . When J_t is ferromagnetic (antiferromagnetic), the β band (α band) with magnetic moment up (moment down) is lowered, which competes with (enhances) the FM band in creating nonequilibrium spin density, δS_z , at the $\text{Cr}_2\text{O}_3/\text{Pt}$ interface.

For linear order in ΔT , we obtain $\delta S_z/\Delta T = \sum_n \int dk_x dk_y \psi_n(N) |\sigma_z| \psi_n(N) \partial_T \rho(\varepsilon_n, T)$, where n is the band index, σ_z is the z component of the Pauli matrices, $N = N_F + N_A$ is the total layer number, $\psi(N)$ locates

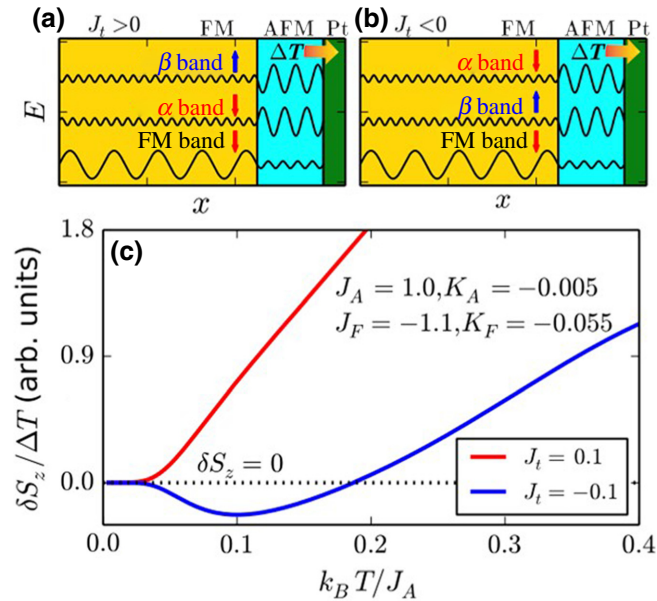


FIG. 7. (a),(b) Schematic magnon-band diagrams and spatial profile of wave functions with positive and negative J_t . Lowest band is the FM band with the moment-down (spin-up) polarization. Wave functions of the FM band are mostly localized inside FM. (c) Nonequilibrium spin accumulation, δS_z , over ΔT at the interface for $J_t = 0.1$ and $J_t = -0.1$. Layer numbers of FM and AFM are $N_F = 30$ and $N_A = 3$, respectively.

the magnon wave function (ψ) at the rightmost interface, and $\rho(\varepsilon, T) = 1/[e^{\varepsilon/k_B T} - 1]$ is the Bose-Einstein distribution. Using typical material parameters, Fig. 7(c) plots the numerical result of $\delta S_z/\Delta T$ as a function of T for two different J_t , which confirms the comparative physical pictures depicted in Figs. 7(a) and 7(b). Specifically, when the exchange coupling is ferromagnetic [$J_t < 0$, see Fig. 7(b)], the β -mode magnons (moment up or spin down) directly compete with the moment-down FM magnons. Because the AFM layer is in direct contact with the Pt layer, the β -mode magnons have a larger probability of interacting with electrons, while the moment-down FM magnons have a larger thermal population because of their lower energy. As the temperature increases, the former becomes more important, which leads to β -mode magnon-dominated negative SSE signals. At higher temperatures, more α -mode magnons are excited, which causes the net polarization to change sign. This interesting temperature dependence of SSE, as represented by $\delta S_z/\Delta T$, is shown by the blue curve in Fig. 7(c). In contrast, if the exchange coupling is antiferromagnetic [$J_t > 0$, see Fig. 7(a)], however, no sign change is predicted, as indicated by the red curve in Fig. 7(c). Our experimental data imply the ferromagnetic interfacial exchange interaction in $\text{YIG}/\text{Cr}_2\text{O}_3$.

VI. CONCLUSION

We demonstrate the ability to efficiently control Cr_2O_3 magnon spin polarization by leveraging the interfacial exchange interaction in $\text{YIG}/\text{Cr}_2\text{O}_3$ heterostructures. The exchange coupling between YIG and Cr_2O_3 with in-plane c -axis orientation splits the AFM magnon bands at zero magnetic field that leads to magnon spin currents produced by both AFM quantum spin states. Our work opens up many exciting possibilities of exploiting the interfacial exchange interaction in FM-AFM heterostructures for controlling spin polarization and ultrafast spin dynamics of AFM materials.

ACKNOWLEDGMENTS

We acknowledge Dr. Krassimir Bozhilov for his help with the HRTEM and EDX characterization. Work at UC Riverside is supported by DOE BES Award No. SC0012670 (Y.W.L., J.X.L., R.C., and J.S.) and DOE BES Award No. DE-FG02-07ER46351 (H.Y.L., W.Y., and J.S.).

- [1] A. V. Chumak, V. I. Vasyuchka, A. A. Serga, and B. Hillebrands, Magnon spintronics, *Nat. Phys.* **11**, 453 (2015).
- [2] L. J. Cornelissen, J. Liu, R. A. Duine, J. B. Youssef, and B. J. Van Wees, Long-distance transport of magnon spin information in a magnetic insulator at room temperature, *Nat. Phys.* **11**, 1022 (2015).

- [3] Y. Kajiwara, K. Harii, S. Takahashi, J. Ohe, K. Uchida, M. Mizuguchi, H. Umezawa, H. Kawai, K. Ando, K. Takanashi, *et al.*, Transmission of electrical signals by spin-wave interconversion in a magnetic insulator, *Nature* **464**, 262 (2010).
- [4] S. Seki, T. Ideue, M. Kubota, Y. Kozuka, R. Takagi, M. Nakamura, Y. Kaneko, M. Kawasaki, and Y. Tokura, Thermal Generation of Spin Current in an Antiferromagnet, *Phys. Rev. Lett.* **115**, 266601 (2015).
- [5] S. M. Wu, W. Zhang, K. C. Amit, P. Borisov, J. E. Pearson, J. S. Jiang, D. Lederman, A. Hoffmann, and A. Bhattacharya, Antiferromagnetic Spin Seebeck Effect, *Phys. Rev. Lett.* **116**, 097204 (2016).
- [6] V. Baltz, A. Manchon, M. Tsoi, T. Moriyama, T. Ono, and Y. Tserkovnyak, Antiferromagnetic spintronics, *Rev. Mod. Phys.* **90**, 015005 (2018).
- [7] P. Němec, M. Fiebig, T. Kampfrath, and A. V. Kimel, Antiferromagnetic opto-spintronics, *Nat. Phys.* **14**, 229 (2018).
- [8] M. B. Jungfleisch, W. Zhang, and A. Hoffmann, Perspectives of antiferromagnetic spintronics, *Phys. Lett. A* **382**, 865 (2018).
- [9] J. Li, Z. Shi, V. H. Ortiz, M. Aldosary, C. Chen, V. Aji, P. Wei, and J. Shi, Spin Seebeck Effect from Antiferromagnetic Magnons and Critical Spin Fluctuations in Epitaxial FeF₂ Films, *Phys. Rev. Lett.* **122**, 217204 (2019).
- [10] J. Li, C. B. Wilson, R. Cheng, M. Lohmann, M. Kavand, W. Yuan, M. Aldosary, N. Agladze, P. Wei, M. S. Sherwin, and J. Shi, Spin current from sub-terahertz-generated antiferromagnetic magnons, *Nature* **578**, 70 (2020).
- [11] P. Vaidya, S. A. Morley, J. van Tol, Y. Liu, R. Cheng, A. Brataas, D. Lederman, and E. del Barco, Subterahertz spin pumping from an insulating antiferromagnet, *Science* **368**, 160 (2020).
- [12] W. Yuan, J. Li, and J. Shi, Spin current generation and detection in uniaxial antiferromagnetic insulators, *Appl. Phys. Lett.* **117**, 100501 (2020).
- [13] D. Reitz, J. Li, W. Yuan, J. Shi, and Y. Tserkovnyak, Spin Seebeck effect near the antiferromagnetic spin-flop transition, *Phys. Rev. B* **102**, 020408 (2020).
- [14] R. Cheng, D. Xiao, and J. G. Zhu, Antiferromagnet-based magnonic spin-transfer torque, *Phys. Rev. B* **98**, 020408 (2018).
- [15] C. Kittel, Theory of antiferromagnetic resonance, *Phys. Rev.* **82**, 565 (1951).
- [16] F. Keffer and C. Kittel, Theory of antiferromagnetic resonance, *Phys. Rev.* **85**, 329 (1952).
- [17] R. Cheng, J. Xiao, Q. Niu, and A. Brataas, Spin Pumping and Spin-Transfer Torques in Antiferromagnets, *Phys. Rev. Lett.* **113**, 057601 (2014).
- [18] Ø. Johansen and A. Brataas, Spin pumping and inverse spin Hall voltages from dynamical antiferromagnets, *Phys. Rev. B* **95**, 220408 (2017).
- [19] J. Nogués and I. K. Schuller, Exchange bias, *J. Magn. Magn. Mater.* **192**, 203 (1999).
- [20] Z. Wang, C. Tang, R. Sachs, Y. Barlas, and J. Shi, Proximity-Induced Ferromagnetism in Graphene Revealed by the Anomalous Hall Effect, *Phys. Rev. Lett.* **114**, 016603 (2015).
- [21] C. Tang, C.-Z. Chang, G. J. Zhao, Y. W. Liu, Z. L. Jiang, C. X. Liu, M. R. McCartney, D. J. Smith, T. Y. Chen, J. S. Moodera, and J. Shi, Above 400-K robust perpendicular ferromagnetic phase in a topological insulator, *Sci. Adv.* **3**, e1700307 (2017).
- [22] F. Katmis, V. Lauter, F. S. Nogueira, B. A. Assaf, M. E. Jamer, P. Wei, B. Satpati, J. W. Freeland, I. Eremin, D. Heiman, *et al.*, A high-temperature ferromagnetic topological insulating phase by proximity coupling, *Nature* **533**, 513 (2016).
- [23] K. L. Seyler, D. Zhong, B. Huang, X. Linpeng, N. P. Wilson, T. Taniguchi, K. Watanabe, W. Yao, X. Xiao, M. A. McGuire, *et al.*, Valley manipulation by optically tuning the magnetic proximity effect in WSe₂/CrI₃ heterostructures, *Nano Lett.* **18**, 3823 (2018).
- [24] F. Wang, D. Xiao, W. Yuan, J. Jiang, Y.-F. Zhao, L. Zhang, Y. Yao, W. Liu, Z. Zhang, C. X. Liu, *et al.*, Observation of interfacial antiferromagnetic coupling between magnetic topological insulator and antiferromagnetic insulator, *Nano Lett.* **19**, 2945 (2019).
- [25] Y. Wu, G. Yin, L. Pan, A. J. Grutter, Q. Pan, A. Lee, D. A. Gilbert, J. A. Borchers, W. Ratcliff II, A. Li, *et al.*, Large exchange splitting in monolayer graphene magnetized by an antiferromagnet, *Nat. Electron.* **3**, 604 (2020).
- [26] M. Lang, M. Montazeri, M. C. Onbasli, X. Kou, Y. Fan, P. Upadhyaya, K. Yao, F. Liu, Y. Jiang, W. Jiang, *et al.*, Proximity induced high-temperature magnetic order in topological insulator-ferrimagnetic insulator heterostructure, *Nano Lett.* **14**, 3459 (2014).
- [27] C. Tang, M. Aldosary, Z. L. Jiang, H. C. Chang, B. Madon, K. Chan, M. Z. Wu, J. E. Garay, and J. Shi, Exquisite growth control and magnetic properties of yttrium iron garnet thin films, *Appl. Phys. Lett.* **108**, 102403 (2016).
- [28] Z. Qiu, D. Hou, J. Barker, K. Yamamoto, O. Gomonay, and E. Saitoh, Spin colossal magnetoresistance in an antiferromagnetic insulator, *Nat. Mater.* **17**, 577 (2018).
- [29] S. M. Rezende, R. L. Rodríguez-Suárez, and A. Azevedo, Theory of the spin Seebeck effect in antiferromagnets, *Phys. Rev. B* **93**, 014425 (2016).
- [30] S. M. Rezende, A. Azevedo, and R. L. Rodríguez-Suárez, Magnon diffusion theory for the spin Seebeck effect in ferromagnetic and antiferromagnetic insulators, *J. Phys. D: Appl. Phys.* **51**, 174004 (2018).
- [31] G. R. Hoogeboom, G.-J. N. Sint Nicolaas, A. Alexander, O. Kuschel, J. Wollschläger, I. Ennen, B. J. van Wees, and T. Kuschel, Role of NiO in the nonlocal spin transport through thin NiO films on Y₃Fe₅O₁₂, *Phys. Rev. B* **103**, 144406 (2021).
- [32] J. Qin, D. Hou, Y. Chen, E. Saitoh, and X. Jin, Crystalline dependence of spin transmission in Cr₂O₃ thin films, *J. Magn. Magn. Mater.* **501**, 166362 (2020).
- [33] P. K. Manna and S. M. Yusuf, Two interface effects: Exchange bias and magnetic proximity, *Phys. Rep.* **535**, 63 (2014).
- [34] S. M. Rezende, A. Azevedo, and R. L. Rodríguez-Suárez, Introduction to antiferromagnetic magnons, *J. Appl. Phys.* **126**, 151101 (2019).
- [35] Y. H. Li and R. Cheng, Moiré magnons in twisted bilayer magnets with collinear order, *Phys. Rev. B* **102**, 094404 (2020).